THE ASTROPHYSICAL JOURNAL, 455:574–589, 1995 December 20

HOT WHITE DWARFS IN THE LOCAL INTERSTELLAR MEDIUM: HYDROGEN AND HELIUM INTERSTELLAR COLUMN DENSITIES AND STELLAR EFFECTIVE TEMPERATURES FROM *EXTREME-ULTRAVIOLET EXPLORER* SPECTROSCOPY

JEAN DUPUIS,[1] STÉPHANE VENNES,[1] AND STUART BOWYER[1]
Center for EUV Astrophysics, 2150 Kittredge Street, University of California, Berkeley, CA 94720–5030
ANIL K. PRADHAN[1]
Department of Astronomy, Ohio State University, Columbus, OH 43210–1106
AND
PETER THEJLL[1]
Niels Bohr Institute, Blegdamsvej 17, DK-2100 Copenhagen, Denmark
Received 1995 April 13; accepted 1995 June 22

ABSTRACT

We have obtained extreme-ultraviolet (EUV) spectra of the hot DA white dwarfs Feige 24, G191-B2B, MCT 0455−2812, HZ 43, GD 71, and GD 153 with the *Extreme-Ultraviolet Explorer* (*EUVE*) observatory. We use these stars as a background against which to perform a study of the local interstellar medium (LISM) absorption. We describe two important instrumental artifacts, fixed pattern noise and overlapping spectral orders, and we develop a methodology to explicitly remove these effects. Feige 24, G191-B2B, and MCT 0455−2812 exhibit a rich complex of heavy element transitions in their otherwise hydrogen-rich photospheres ($Z \approx 10^{-5}$), while HZ 43, GD 71, and GD 153 are consistent with hydrogen atmospheres with a low metallicity ($Z \leq 10^{-7}$). The photoionization edge of interstellar He I at 504 Å is clearly detected in the spectra of each of these white dwarfs. We have analyzed the EUV continuum spectra of these stars with a grid of pure-hydrogen model atmospheres and, in the case of Feige 24, G191-B2B, and MCT 0455−2812, with a grid of models incorporating new opacities of C, N, O, and Fe from the Opacity Project. We obtain new EUV continuum-based estimates of effective temperatures for our sample stars and, for the three high-metallicity white dwarfs, we establish the effects of heavy element blanketing on the EUV continuum of these objects and on the determination of effective temperatures. We find that the ratio of the neutral column densities of hydrogen and helium in the LISM is similar ($n_{\rm H\,I}/n_{\rm He\,I} \approx 14$) for five out of six stars in the sample but that Feige 24 may have a substantially different value. The Feige 24 results suggest that the ionization state in the LISM is inhomogeneous. Our measurements favor a higher degree of ionization of helium relative to hydrogen and also indicate that hydrogen in the LISM is predominantly neutral in at least two lines of sight.

Subject headings: ISM: abundances — ISM: structure — ultraviolet: stars — white dwarfs

1. INTRODUCTION

The *Extreme-Ultraviolet Explorer* (*EUVE*) all-sky survey (Bowyer et al. 1994) has revealed numerous hot white dwarf stars as extreme-ultraviolet (EUV) sources. These objects are among the brightest EUV sources cataloged and are located at distances from a few parsecs up to several hundred parsecs. These sources are ideal for a study of the abundance of helium and hydrogen in the local interstellar medium (LISM). Few EUV spectra of white dwarf stars were obtained before *EUVE*'s advent. The sounding rocket experiment of Green, Jelinsky, & Bowyer (1990) produced the first EUV spectrum of G191-B2B extending shortward of the neutral helium photoionization edge up to the Lyman edge. From this spectrum it was concluded that hydrogen cannot be strongly ionized (≤40%) in the LISM, a result at odds with a class of exotic models predicting a higher degree of ionization (e.g., Sciama 1991). This result was later confirmed by an observation of G191-B2B by the Hopkins Ultraviolet Telescope (HUT) (Kimble et al. 1993a), which produced a higher resolution and signal-to-noise ratio spectrum with an obvious detection of the neutral helium edge. Observations by HUT (Kimble et al. 1993b) also invalidate the anomalous but nonetheless attractive result of the strong ionization of hydrogen relative to helium in the line of sight of HZ 43 (Heise et al. 1988) required to match the *EXOSAT* and *Voyager* spectra of that object (Holberg et al. 1980). Models of the ionization of hydrogen and helium in the ISM were proposed in various investigations (e.g., Reynolds 1986; Slavin 1989; Cheng & Bruhweiler 1990). These investigations were potentially hampered by insufficient knowledge of the *actual* EUV/soft X-ray radiation field. In particular, major sources of photoionization discovered with *EUVE* were not included in these models. It is important to establish whether or not the same degree of ionization is measured for other lines of sight indicating an isotropy in the physical conditions reigning in the local ISM, in particular the ionizing radiation field. Direct determinations of the cosmic abundance ratio of hydrogen and helium are difficult to obtain but have implications for cosmological models.

Hot white dwarfs are bright Lyman-continuum sources, as indicated by their detection in two *EUVE* survey bandpasses, the 400 Å (10% bandpass: 345–605 Å) and 600 Å filter bands (10% bandpass: 500–740 Å). Vennes et al. (1994) have demonstrated that *EUVE* photometry can effectively constrain the star's effective temperature as well as the LISM hydrogen column density. They have presented an analysis of a subsample of those white dwarfs that show a low hydrogen

---

[1] Guest observer, NASA's *Extreme-Ultraviolet Explorer*.

column density ($\leq 3 \times 10^{18}$ cm^{-2}) and put a lower limit on the extent of a neutral cloud, known as the "local fluff," surrounding the Sun. The long-wavelength observations, where photoelectric absorption by interstellar neutral hydrogen is the most severe, are the most constraining. Following Vennes et al. (1994), we analyze spectroscopic observations obtained with *EUVE* for six of the hot H-rich white dwarf stars (DA) detected in the Lyman continuum. In general, EUV photometry can only constrain the effective temperature and the hydrogen column density of these objects, but EUV spectroscopy provides, in addition, a determination of the neutral helium column density and, therefore, the relative degree of ionization of hydrogen and helium along their lines of sight. Furthermore, the photoionization edge of singly ionized helium at 228 Å *and* the neutral helium autoionization transition at 206 Å were detected in the white dwarf GD 246 (Vennes et al. 1993); from this detection, a direct measurement of the degree of ionization of helium (25%) and an upper limit on the degree of ionization of hydrogen (<27%) was obtained, and similar results may be achieved with observations of additional white dwarfs.

As part of NASA's *EUVE* Guest Observer Program, we have obtained high signal-to-noise EUV spectra of the hot DA stars Feige 24, G191-B2B, GD 71, GD 153, HZ 43, and MCT 0455−2812. In § 2 we introduce the observations acquired with the *EUVE* spectrometer emphasizing the 504 Å photoionization edge of neutral helium and the Lyman continuum of hydrogen. We describe an observation technique ("dithering") that substitutes for usual detector flat-fielding techniques that are not practical for use with the *EUVE* spectrometers. An important issue also addressed in this section is the calibration of the effective areas of the *EUVE* spectrometer in the first and second orders. In § 3, we present the column density measurements (§ 3.2), and we explore the sensitivity to effective temperature and surface gravity; we also present estimates of the degree of hydrogen and helium ionization (§ 3.3). Finally, we ascertain the sensitivity of the EUV continua to the chemical composition and the effects on effective temperature determinations (§ 3.4). We summarize our results in § 4.

2. OBSERVATION AND DATA REDUCTION

The data were obtained with spectrometers on board the *EUVE* observatory. The instrument is composed of a Wolter-Swarzschild type II grazing incidence telescope in which half the light is imaged on the Deep Sky Survey EUV photometer and the other half is directed to three medium-resolution ($\lambda/\Delta\lambda \approx 200$) variable line-spaced gratings: short-wavelength or "SW" (70–190 Å), medium-wavelength or "MW" (140–380 Å), and long-wavelength or "LW" (280–760 Å). Refer to Hettrick et al. (1985) and to the *EUVE* guest observer's handbook for a more detailed description of the spectrometer. The stars studied here are all white dwarfs selected as calibration targets but for which we were also granted data rights as guest observers. A summary of the observing dates, exposure times, and other relevant information is provided in Table 1. A special observing technique, labeled "dithering," was tried during the most recent observations of HZ 43, Feige 24, and G191–B2B (see the last entry in Table 1 for exact dates of the dithered observations), and the observation of MCT 0455−2812. This procedure has proven effective in reducing fixed pattern noise in the detectors. Appendix A describes the dithering technique in greater detail.

The data were processed and reduced with the help of the standard EUV software package (version 1.3) in IRAF provided by the *EUVE* Guest Observer Center at the University of California, Berkeley. All the data were reprocessed with the egodata 1.8 version of the wavelength solution. We filtered the data to eliminate high background intervals and corrected for instrumental deadtime and telemetry saturation with the various programs found in the EUV package as prescribed in the *EUVE* Guest Observer Guide. Because the nominal extraction provided to guest observers neglects the presence of a noticeable curvature in the spectral trace and substantial deviations of its location from the image center, we have reextracted the spectra using standard IRAF procedures. We averaged and subtracted the background selected in areas located between 20 and 70 pixels above and below the spectral trace and extracted the spectra from wavelength-calibrated images. Several of the observations are separated in two or more segments that were separated by several months. After verifying the stability of the throughput and the spectra wavelength alignment over these timescales, we co-added the spectra to improve the signal-to-noise ratio. In Figure 1 we show the complete EUV energy distributions of the stars in the sample on a photon flux scale, and Figure 2 presents a closer view of the He I and He II photoionization edge regions. We indicate locations of the helium photoionization edges near 228 and 504 Å, and we will discuss this aspect further in §§ 3.2 and 3.3.

The spectra are separated in two groups characterized by different metallicity (Z), the high-Z ($\approx 10^{-5}$) group including G191-B2B, MCT 0455−2812, and Feige 24 in the upper panel and the low-Z ($\leq 10^{-7}$) group with HZ 43, GD 153, and GD 71 in the lower panel. The distinctively different spectral shapes

TABLE 1

EUVE OBSERVING LOG FOR THE SELECTED SAMPLE OF HOT DA STARS

Name	Observation	Exposure Times for SW, MW, and LW (10^3 s)	Number of Dithers
Feige 24	1993 Nov 25 at 16:01:00	26.6, 26.0, 25.0	13
G191-B2B	1993 Oct 28 at 18:06:20	58.8, 49.3 60.8	32
	1993 Dec 7 at 18:47:00	27.7, 20.6, 26.5	13
GD 71	1993 Jan 10 at 00:00:00	57.5, 59.7, 57.9	...
GD 153	1993 Feb 9 at 08:10:00	79.3, 77.8, 74.6	...
	1993 Mar 4 at 00:14:24	26.6, 24.3, 25.1	...
	1993 Mar 5 at 11:45:36	30.7, 30.7, 28.7	...
HZ 43	1994 Mar 25 at 23:12:00	32.3, 31.1, 30.6	8
	1994 Mar 28 at 19:05:00	39.9, 36.7, 38.0	8
	1994 May 20 at 22:27:00	70.7, 63.3, 64.4	15
MCT 0455−2812	1993 Nov 14 at 21:33:00	56.6, 49.2, 56.1	27

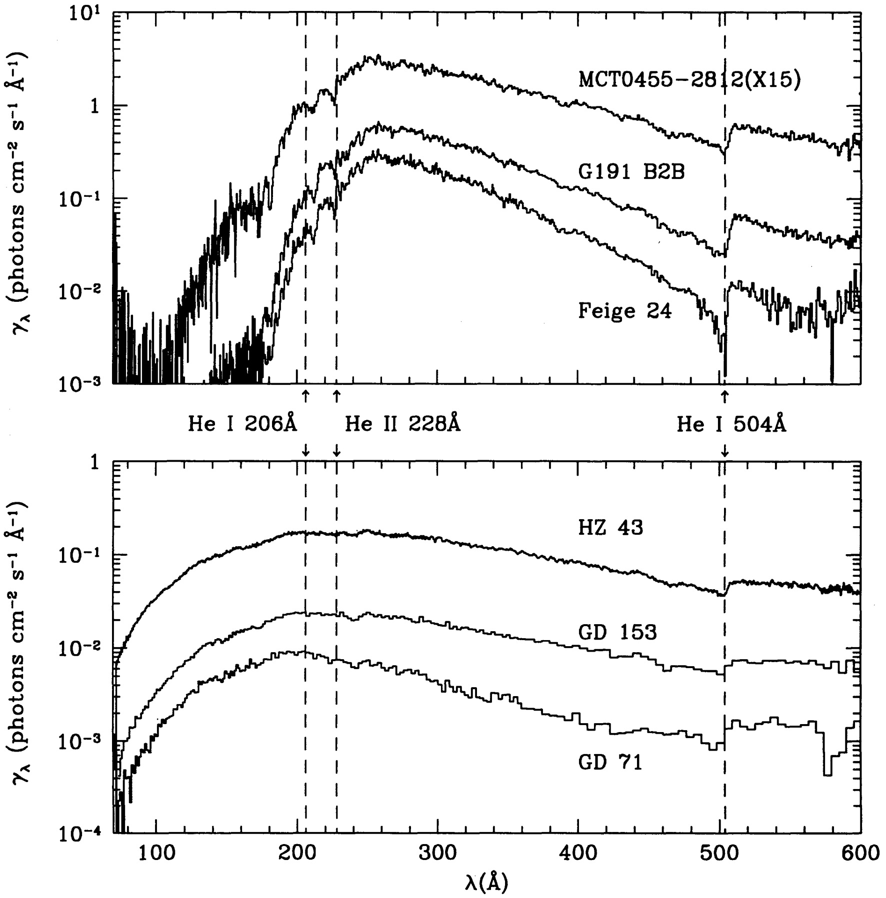

FIG. 1.—*EUVE* spectra of the hot DA stars studied in our sample. The main spectral features from the ISM are marked with *vertical dotted lines*. *Top*: Three stars in the sample with strong heavy element contamination are shown. Note the striking flux deficiency at wavelengths shorter than 250 Å compared to the remaining stars in the sample (*bottom*) having a much lower metallicity. The spectra are order-subtracted and flux calibrated.

of the two white dwarf groups are mainly caused by heavy element opacities absorbing the EUV flux shortward of 240 Å. G191-B2B, MCT 0455−2812, and Feige 24 look remarkably alike; they exhibit almost all the same absorption features with very comparable strengths, suggesting similar photospheric abundances of metals. It is also clear that helium does not appear to be a dominant source of photospheric opacity, as the ground state series of He II is notably absent. We note the absence of helium lines in the three low-*Z* objects. The HZ 43 spectrum exhibits very weak absorption features possibly produced by a low level of metal contamination or a residual of fixed pattern noise. A detailed discussion of fixed pattern noise is provided in Appendix A. The absorption edge at 504 Å associated with photoionization of neutral helium in the local interstellar medium is another important feature of the spectra. The location of the photoionization edge of singly ionized helium is also indicated with a possible detection in Feige 24, MCT 0455−2812, and G191-B2B.

We had to take into account the important instrumental effect of spectral contamination from overlapping spectral orders. This consideration is important for this work, since near the He I λ504 edge a substantial contribution by second and third orders is expected in the LW spectrometer using preflight estimates of the effective areas. Therefore, we have *established* these effective areas empirically using the LW spectra of suitable objects. Details on this work are found in Appendix B.

3. ANALYSIS

The objectives of the analysis are to determine the column density of He I through a measurement of the 504 Å edge and to constrain the column density of H I by fitting the white dwarf continuum in the LW spectrometer. In addition, we have searched for the He II edge in the MW spectrometer. We use the EUV spectra to refine the effective temperature measurements, and we provide LISM column densities of H I and He I consistent with these improved atmospheric parameters.

3.1. *White Dwarf Model Atmospheres and Synthetic Spectra*

As a first step, all spectra are analyzed with synthetic spectra of pure hydrogen white dwarf atmospheres (Vennes 1992). The models include the effect of H I Balmer and Lyman line blanketing. In the case of Feige 24, G191-B2B, and MCT 0455−2812, these models are possibly inappropriate, particularly at shorter wavelengths where heavy element opacities presumably cause large departures from a pure hydrogen spectrum. The influence of heavy elements is demonstrated in Figure 1, where we compare the high- and low-*Z* stars. We computed model atmospheres in radiative equilibrium including opacities of a mixture of heavy elements. The opacities are

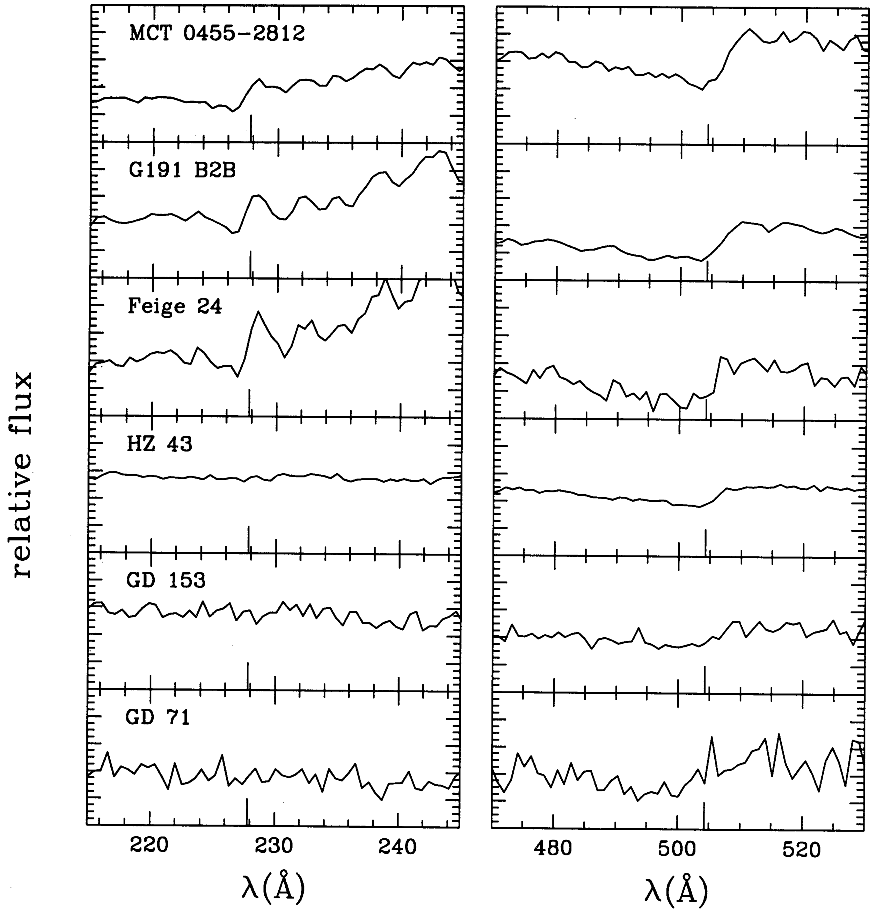

FIG. 2.—Enlargement of the spectra shown in Fig. 1 around the He II edge (228 Å) and the He I edge (504 Å) for the five stars in the sample. The locations of both edges are indicated by the long *vertical tick marks.*

tabulated at a given electron density and effective temperature (n_e, $T_{\rm eff}$) and include bound-bound and bound-free transitions of H, C, N, O, and Fe (Vennes, Pradhan, & Thejll 1995) using new radiative cross sections from the Opacity Project (Seaton et al. 1994). The abundances are fixed according to various analyses of *IUE* high-dispersion spectra: C/H = 4×10^{-7}, N/H = 5×10^{-6} (Vennes, Thejll, & Shipman 1991), O/H = 10^{-6} (Chayer & Vennes 1995), and Fe/H = 10^{-5} (Vennes et al. 1992). We have determined that for the estimated metal abundances of the three high-*Z* stars, the difference from a pure hydrogen spectrum is significant while for 10 times lower metal abundance, it is not. Therefore, we model only the three high-*Z* white dwarfs with metal-blanketed model atmospheres, and we use pure hydrogen models for the three low-*Z* stars.

3.2. *Interstellar Column Densities of* H I, He I, *and* He II *Based on Pure Hydrogen Models*

The determination of the neutral helium column density may be obtained directly from a fit to the shape of the well-defined He I λ504 photoionization edge; the measurement of *N* (He I) is model independent and nearly decoupled from other parameters [e.g., *N*(H I) and $T_{\rm eff}$]. The neutral hydrogen column density may be obtained from a fit to the continuum and is intimately coupled to the effective temperature measurement. It is also sensitive to the absolute flux calibration. In principle, the ionized helium column density may be obtained from a fit to the He II 228 Å edge; however, the feature is possibly blended with heavy element opacities in some high-*Z* objects (Fig. 1). Therefore, we follow a three-step procedure taking advantage of the presence of well-defined spectroscopic features (e.g., He I λ504 and He II λ228 edges). (1) We determine *N*(He I) by fitting the He I λ504 edge within a narrow band, 40 Å wide centered on the edge, such that χ^2 is dominated by the shape of the edge. To provide an adjustment to the continuum level, we allow *N*(H I) to vary simultaneously while $T_{\rm eff}$ is fixed. The model spectra used for these fits have atmospheric parameters based on UV or optical observations (Holberg, Wesemael, & Basile 1986; Vennes 1992; Bergeron et al. 1994). (2) Fixing *N*(He I) to its best value, we simultaneously determine *N*(H I) and $T_{\rm eff}$ over a broad continuum range (150 Å). (3) Finally, we constrain the ionized helium column density independently from the other parameters.

In the course of the analysis, we noted that the shape of the helium edge at 504.279 Å was much less sharp than can be accounted for by a pure step function, which should be representative of a photoionization process. Therefore, we modeled the shape of the edge by including the convergent lines of the ground-state series of neutral helium in the interstellar medium. We have used the first hundred ground-state lines represented by Voigt profiles at an LISM kinetic temperature of 8000 K, a value consistent with the one obtained by Hurwitz & Bowyer (1995). The values of the oscillator strengths were obtained from the tables of Theodosiou (1987) for the $1s(^1S)$–$np(^1P)$ transitions where $n \leq 21$. For the remaining levels, we

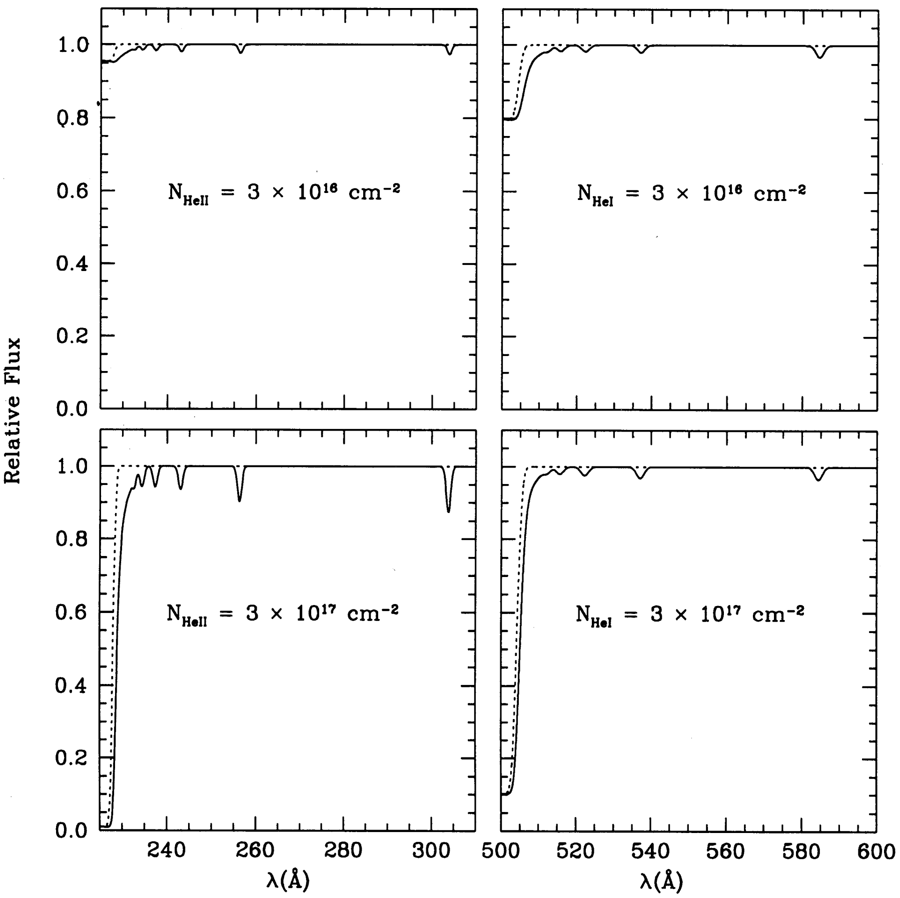

FIG. 3.—Effect of interstellar helium absorption lines on the shape of the photoionization edges of neutral and singly ionized helium as observed by *EUVE*. When these effects are included, the lines produce much less sharper He I and He II edges than for the case without lines (*dashed curves*).

scaled hydrogenic *f*-values. We found that the shape of the edge varies only weakly over a broad range of temperatures. At *EUVE*'s spectral resolution, lines near the series limit are not resolved, but their convergence results in an observable flattening of the edge. This effect is illustrated in Figure 3 (*right panels*) for typical column He I densities. The observed flattening does not provide a sensitive probe of the temperature of the LISM. We have similarly modeled the He II edge including the first hundred lines of the ground state series. We illustrate this effect in Figure 3 (*left panels*). At low column densities, the edge is almost completely flattened, which may contribute to masking a significant amount of He II in some low-density LISM lines of sight.

In the first step of our procedure, we generated grids of synthetic spectra (at given $T_{\rm eff}$ and log g) over ranges of hydrogen and neutral helium column densities guided by the values derived from *EUVE* photometry (Vennes et al. 1994). Each model is multiplied by the ISM transmission computed using the Rumph, Bowyer, & Vennes (1994) absorption cross sections at the grid values of the H I and He I column densities. Finally, we convolved our models with the spectrometer response (approximated by a Gaussian with a standard deviation of 1 Å for the LW spectrometer and 0.5 Å for the MW spectrometer) and normalized them to the *V* magnitude of the star. Typically 30 points per dex of H I and He I column densities are required in the grid to provide good accuracy in the subsequent calculations. The H I and He I column densities that best fit the observed spectra are determined by searching the grid for the combination of parameters minimizing the χ^2. The best fits are shown along the observed spectra in Figures 4*a*–4*e* with the confidence levels of 68.3%, 95.4%, and 99.73%. These levels were computed using the Lampton, Margon, & Bowyer (1976) prescription for a two-parameter fit. In order to improve the signal-to-noise ratio, the spectra were rebinned over half a resolution element (about 1 Å in the LW) for HZ 43 and G191-B2B. For the other stars, the spectra were rebinned over two (Feige 24 and GD 153) and five (GD 71) resolution elements because their spectra are noisier in the LW spectrometer. We list the results for the He I column densities in Table 2 along with the 1 σ error bars computed from the confidence contours. As mentioned earlier in this section, these fits are mainly aimed at fixing the He I columns even if the H I columns are also determined. However, the H I columns do not correspond to values consistent over a larger extent of the Lyman continuum and to the effective temperatures in agreement with the *EUVE* spectra. This question is considered next.

EUVE spectroscopy also provides independent constraints on the effective temperature that can be contrasted with determinations based on Balmer line spectroscopy and *IUE* spectrophotometry. We have determined that surface gravity variations over 1 order of magnitude do not significantly affect the Lyman continua of hot white dwarf stars near 500 Å. For

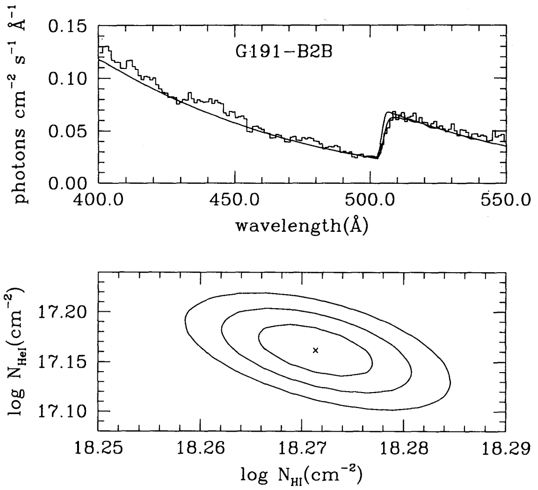

FIG. 4*a*

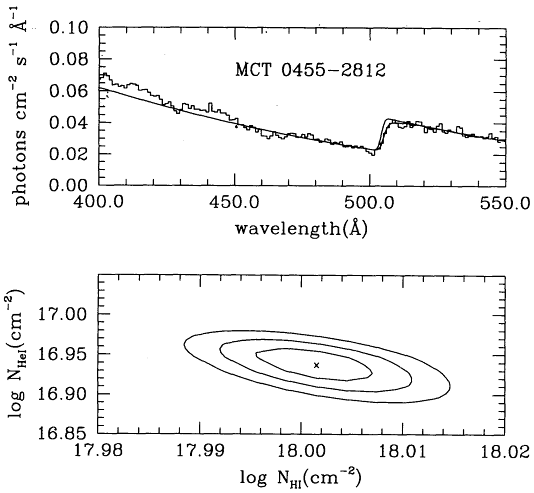

FIG. 4*b*

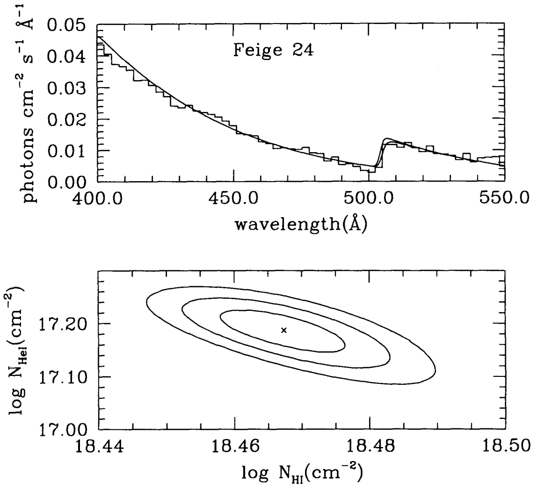

FIG. 4*c*

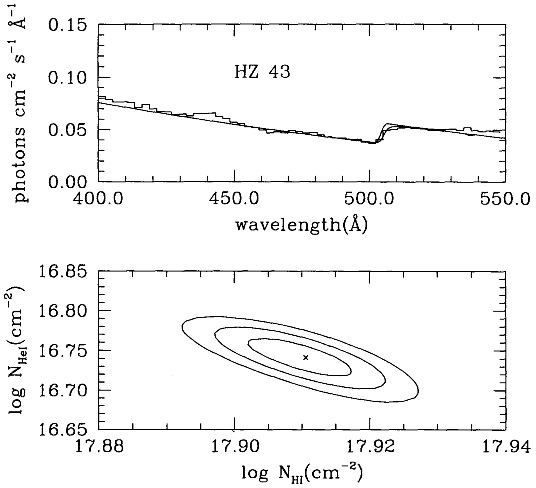

FIG. 4*d*

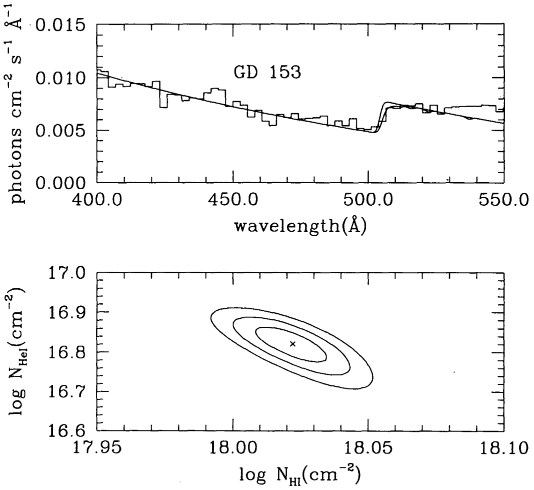

FIG. 4*e*

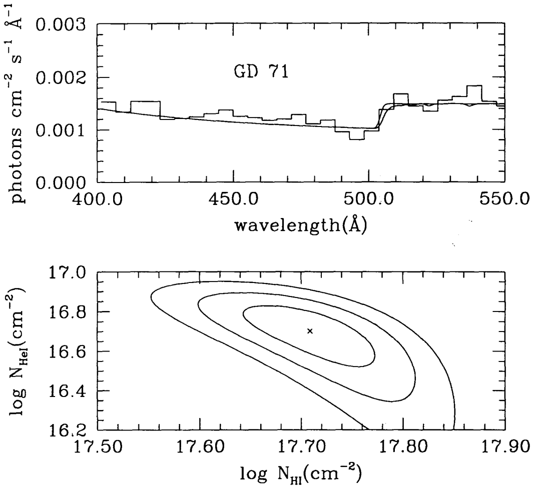

FIG. 4*f*

FIG. 4.—(*a*) Minimum χ^2 fit of the ISM photoionization edge of He I at 504 Å and continuum absorption of H I in the line of sight of G191-B2B. *Top*: We present two model fits to the *EUVE* spectrum, one excluding the effect of ISM He I absorption lines and the other including them; the model including interstellar absorption lines of helium provides a superior fit of the edge (*bottom*). Contours of constant χ^2 corresponding to 1, 2, and 3 σ are displayed. The best solution is shown with a *cross*. (*b*)–(*f*) Same as (*a*) but for MCT 0455−2812, Feige 24, HZ 43, GD 153, and GD 71.

1995ApJ...455..574D

TABLE 2

INTERSTELLAR NEUTRAL HYDROGEN AND HELIUM COLUMN DENSITIES IN THE LINE OF SIGHT

Name	Model	N(H I) (10^{17} cm^{-2})	N(He I) (10^{17} cm^{-2})	N(He I)/N(H I)
Feige 24	pure-H	28.3 ± 0.8	1.54 ± 0.14	0.055 ± 0.005
	H+CNOFe	30.0 ± 0.7	1.63 ± 0.11	0.054 ± 0.004
G191-B2B	pure-H	19.0 ± 0.7	1.46 ± 0.08	0.077 ± 0.005
	H+CNOFe	20.7 ± 0.4	1.50 ± 0.08	0.072 ± 0.004
MCT 0455−2812	pure-H	11.4 ± 0.5	0.87 ± 0.04	0.076 ± 0.005
	H+CNOFe	12.9 ± 0.4	0.95 ± 0.03	0.075 ± 0.003
GD 153	pure-H	9.8 ± 0.8	0.66 ± 0.07	0.067 ± 0.009
HZ 43	pure-H	8.7 ± 0.6	0.55 ± 0.03	0.063 ± 0.006
GD 71	pure-H	6.3 ± 1.6	0.52 ± 0.08	0.083 ± 0.025

instance, the difference between the best-fit column densities of H I obtained with models of log g equal to 7 and 9 is about 2% for HZ 43.

We determined the effective temperature and the LISM H I column density simultaneously, fixing the He I column density to the best value and subsequently to its upper and lower bounds. We use the same technique as for the He I edge, but covering the continuum between 400 and 550 Å. This spectral region is less affected by heavy element opacities or uncertainties in surface gravity. Generally, the best-fit hydrogen columns are consistent with those obtained when fixing the effective temperature, but the uncertainties on the H I column density and effective temperature measurements are determined simultaneously. In Figures 5*a*–5*e* we show the results of our analysis for He I column densities fixed to the best-fit values. The corresponding LISM neutral hydrogen and helium columns now complete Table 2. The effective temperatures are given in Table 3 along with Galactic coordinates and distance estimates. The error bars on the H I column density and effective temperature measurements make allowance for the quoted uncertainties on the He I column density. These new effective temperature estimates compare well with the results of the analysis of *EUVE* photometry by Vennes et al. (1994) but are much more accurate. The uncertainties of the effective temperatures are comparable to determinations based on Balmer line spectroscopy and *IUE* spectroscopy (see Table 3), but systematic errors introduced by uncertainties in the absolute instrumental calibration add an additional source of error. Optical spectroscopy also suffers from substantial calibration problems. Bergeron et al. (1994), based on multiple measurements of selected white dwarfs (Feige 55, LS V+46 21), have stressed the fact that external sources of uncertainties such as the flux calibration can dominate the internal precision provided by Balmer line fits. We consider our new estimates of white dwarf effective temperatures as an important result of our analysis of *EUVE* spectroscopy.

The error bars on column density and temperature measurements (Tables 2 and 3) take into account small-scale systematic errors caused by either missing opacities in the models or residual fixed-pattern noise; we adjusted empirically our estimates of the signal-to-noise ratio (standard deviation) taking into account local deviations between models and spectra exceeding the statistical noise. We have also investigated the potential impact of a systematic uncertainty on the absolute calibration of the effective area of the LW spectrometer by reducing and decreasing the effective areas by 20%, a conservative estimate of the uncertainty on the absolute level of the effective areas. We have determined that the shifts introduced by this adjustment on effective temperature and hydrogen column density measurements are, respectively, of the order of 3% and 10% of the values obtained using the nominal effective areas. For example, G191-B2B's effective temperature would be adjusted by ±1200 K, and the neutral hydrogen column density would be adjusted by $\pm 0.11 \times 10^{18}$ cm^{-2}, including this additional source of error. The precision in the determination of ratios of He I to H I column densities remains excellent.

Contamination of the first-order spectrum by higher overlapping spectral orders in the LW spectrometer presents an additional source of error. This problem is discussed in detail in Appendix B, where we derive an empirical correction to the preflight high-order effective areas. For the three high-Z stars,

TABLE 3

PARAMETERS OF THE HOT DA STARS

Name	l	b	d (pc)	Model	$T_{\rm eff}$ (optical, UV) (10^3 K)	$T_{\rm eff}$ (EUV) (10^3 K)
MCT 0455−2812	229°.3	−36°.2	90	pure-H	60.7[a]	68.7 ± 1.3
				H+CNOFe	...	63.4 ± 0.9
Feige 24	166.0	−50.3	90	pure-H	54.0[b]	63.1 ± 1.9
				H+CNOFe	...	58.7 ± 0.9
G191-B2B	156.0	+7.1	48	pure-H	55.7,[b] 64.1[c]	57.9 ± 1.5
				H+CNOFe	...	54.0 ± 0.8
HZ 43	54.2	+84.2	63	pure-H	50.0,[b] 49.0[d]	51.1 ± 0.5
GD 153	317.3	+84.8	69	pure-H	41.2,[b] 40.0[c]	39.7 ± 0.3
GD 71	192.0	−5.3	42	pure-H	32.8,[b] 33.6[c]	32.4 ± 0.5

[a] Barstow et al. 1994.

[b] Vennes 1992.

[c] Bergeron et al. 1994.

[d] Napiwotzki et al. 1993.

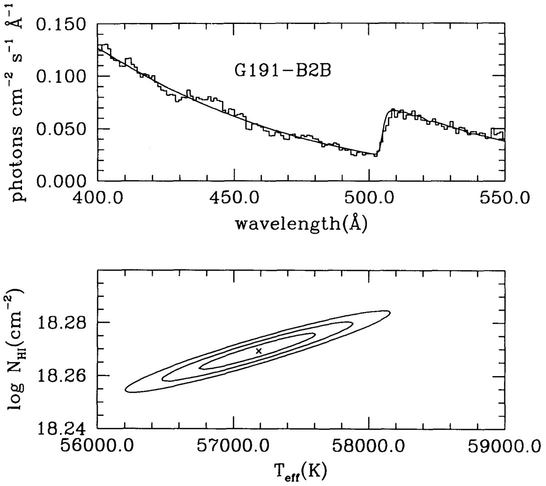

FIG. 5*a*

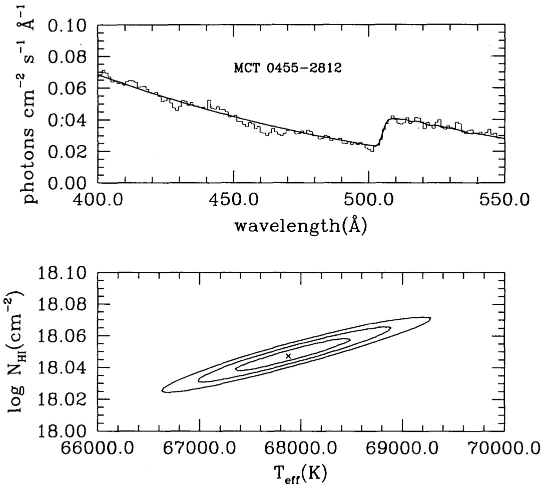

FIG. 5*b*

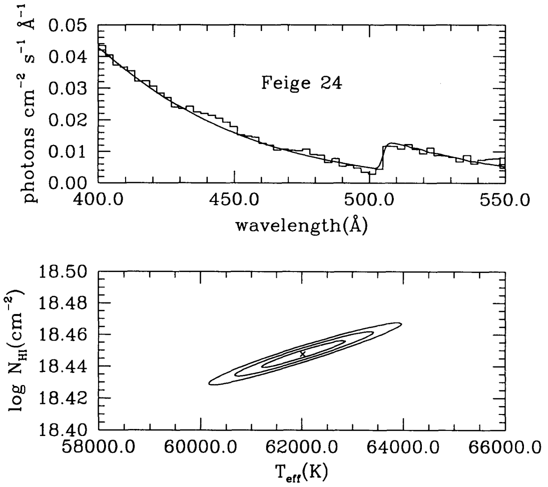

FIG. 5*c*

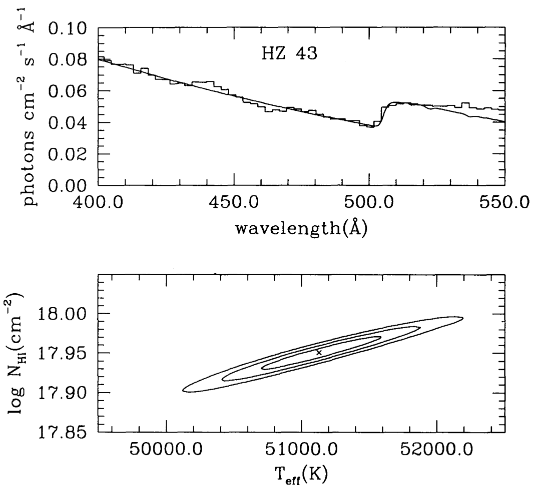

FIG. 5*d*

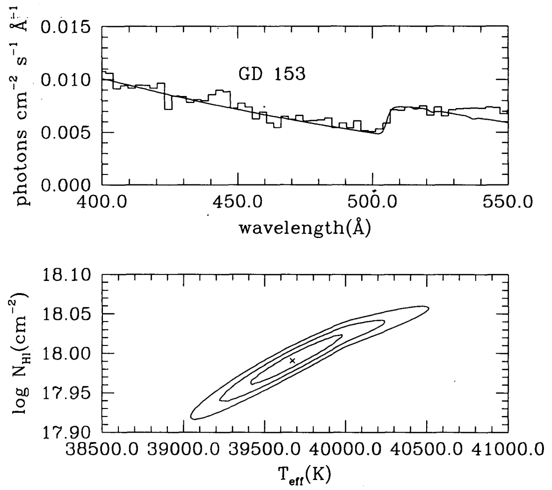

FIG. 5*e*

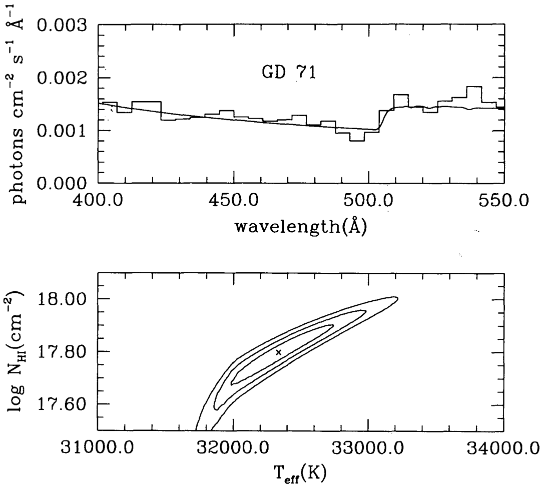

FIG. 5*f*

FIG. 5.—(*a*) Minimum χ^2 fit of the Lyman continuum of G191-B2B from 400 to 600 Å using pure hydrogen models and fixing the neutral helium column density to the best fit (Fig. 4*a*). We present (*top*) two model fits to the *EUVE* spectrum, one excluding the effect of ISM He I absorption and the other including it. Finally, we present (*bottom*) contours of constant χ^2 corresponding to 1, 2, and 3 σ. The best solution is shown with a *cross*. (*b*–*f*) Same as (*a*), but for MCT 0455 − 2812, Feige 24, HZ 43, GD 153, and GD 71.

the spectra in the range surrounding the 504 Å edge are mainly contaminated by the second order. The third-order contribution is small, since the stellar flux is suppressed below 200 Å in those stars. We estimate the second-order contribution to be at most 50% of the total counts at the 504 Å edge. The error of the second-order contribution is about 10%, and we have calculated that this would result in a 2% error in the He I column density measurement. For the three pure hydrogen white dwarfs, the contribution of the third order is more important because the stellar fluxes extend to shorter EUV wavelengths. Fortunately, the third order becomes important at wavelengths longer than 510 Å (location of the 170 Å aluminum edge in third order) and leaves the 504 Å relatively clear of third-order contamination. We have verified that the contribution of the sum of the second and third orders does not exceed 30%. We conclude that the error on the He I column density measurement associated with the subtraction of high spectral orders will be smaller than 2% in the three pure hydrogen white dwarfs.

Our sample of column measurements indicates a relatively constant $n_{\mathrm{H\,I}}/n_{\mathrm{He\,I}}$ ratio of 14, with a possible excess in the case of Feige 24's line of sight. What can be learned from our sample of stars about the distribution of ionized gas in the local interstellar medium? We present in Figure 6 the He I column densities as a function of the H I column densities, and we compare with lines of constant N(He I)/N(H I) ratios (from 0.05 to 0.1). The ratio of neutral helium to hydrogen does not correlate with column density or distance. However, at the largest column density and distance set by Feige 24 ($d \approx 100$ pc), a significant departure from a monotonic relation is noticeable.

3.3. *Ionization of Helium and Hydrogen in the LISM*

An estimate of the relative ionization of helium and hydrogen in the LISM is obtained from a comparison with the ratio of the sum of all ionization species of hydrogen to helium. We assume the canonical cosmic abundance ratio of helium to hydrogen of 0.1 (Grevesse & Noels 1993). Ionization of hydrogen and helium would be noticeable in a deviation of the measured ratio of the neutral species from the cosmic abundance ratio.

We constrain further the helium ionization level, f_{He}, by setting a limit on the column of He II using the He II $\lambda 228$ photoionization edge. We assume that doubly ionized helium does not contribute significantly to the ionization balance; we provide below some evidences that this is the case. Two important effects suggest caution: (1) ionized helium ground-state absorption features are possibly blended with heavier element transitions, and (2) at low column densities, the He II photoionization edge is partly diluted by convergence of the ground-state line series. Therefore, we have determined a 3 σ upper limit to the ionized helium column density in all lines of sight based on the continuum shape close to $\lambda = 227.84$ Å. Interestingly, both Feige 24 and G191-B2B, the two objects in our sample with the largest column density, display a strong continuum dip near the expected position of the He II absorption edge; the shape of the feature is also consistent with a sharp, unresolved edge possibly characteristic of absorption in low-density material. We present in Table 4 the upper limits to the ionized helium column densities with the corresponding upper limits to the helium ionization fractions. These upper limits are consistent with the ionization fraction measured in the line of

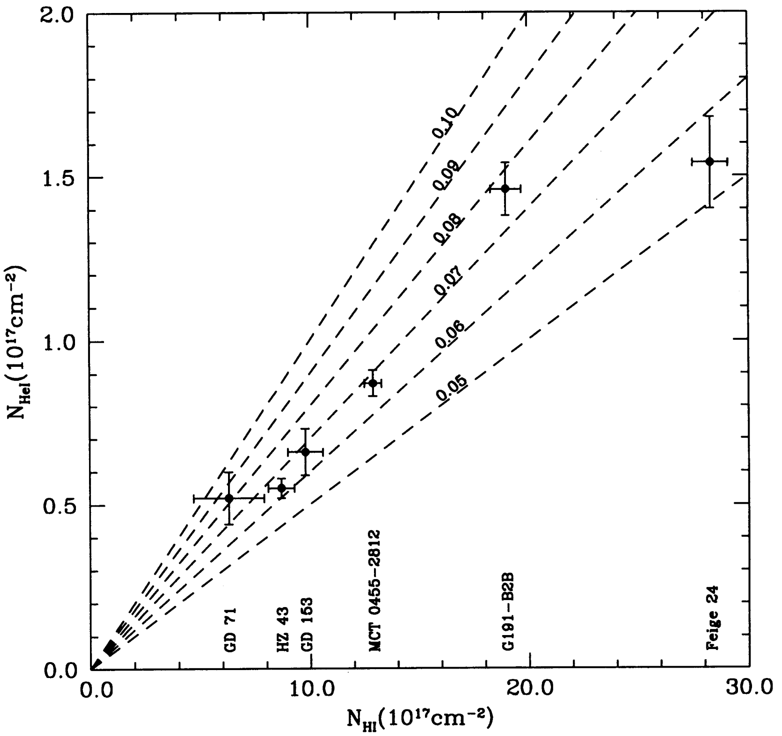

FIG. 6.—Ratios of He I/H I in the ISM for the lines of sight of the white dwarfs in the sample. Straight lines trace loci of constant He I/H I ratios. All stars in the sample are consistent with a ratio well below the canonical cosmic value of 0.1 for the ratio of helium abundance relative to that of hydrogen.

TABLE 4

UPPER LIMITS TO THE HELIUM IONIZATION FRACTION IN THE LINE OF SIGHT

NAME	N(He II) (10^{17} cm^{-2})	N(He I)[a] (10^{17} cm^{-2})	N(He II) / [N(He I) + N(He II)]
Feige 24	<6.6	1.54 ± 0.14	<0.8
G191-B2B	<4.5	1.46 ± 0.08	<0.8
MCT 0455−2812	<4.1	0.87 ± 0.04	<0.8
GD 153	<1.0	0.66 ± 0.07	<0.6
HZ 43	<0.7	0.55 ± 0.03	<0.5
GD 71	<1.0	0.52 ± 0.08	<0.6

[a] From Table 2.

TABLE 5

UPPER LIMITS TO THE HYDROGEN IONIZATION FRACTION

NAME	N(H I)[a] (10^{17} cm^{-2})	N(H)[b] (10^{17} cm^{-2})	N(H II) / [N(H I) + N(H II)]
Feige 24	28.3 ± 0.8	<81	<0.7
G191-B2B	19.0 ± 0.7	<60	<0.7
MCT 0455−2812	11.4 ± 0.4	<50	<0.8
GD 153	9.8 ± 0.8	<17	<0.5
HZ 43	8.7 ± 0.6	<13	<0.4
GD 71	6.4 ± 1.6	<15	<0.7

[a] From Table 2.

[b] Scaled from the total helium column (Table 4) and assuming a cosmic abundance ratio $N(\mathrm{H})/N(\mathrm{He}) = 10$.

sight of GD 246 (Vennes et al. 1993) but do not rule out a higher or lower degree of ionization of helium in the LISM.

The sum of the neutral helium column density and of the upper limit to the ionized helium column density can therefore set an upper limit to the total helium column density, and assuming a cosmic hydrogen to helium abundance ratio of 10, we determine an upper limit to the *total hydrogen column density*. Table 5 shows a comparison of the *measured* neutral hydrogen column density and the *projected* total hydrogen column for our sample. Using these data, we can set upper limits to the degree of ionization of hydrogen, f_{H}, in those lines of sight. Hydrogen could be up to 70% ionized in four lines of sight, but an upper limit of $f_{\mathrm{H}} \leq 30\%$–50% is set in the cases of HZ 43 and GD 153. We conclude that a high hydrogen ionization level is not a general property of the LISM. A similar result was derived from observations of the white dwarf GD 246 (Vennes et al. 1993), and the present conclusion conflicts with indirect measurements of the hydrogen ionization level based on the Mg II/Mg I ionization ratio (e.g., Lallement et al. 1994; Frisch et al. 1990) that suggests a much higher ionization level.

Finally, we estimate the contribution of our sample white dwarfs to the ambient ionizing radiation in the Sun's vicinity. In Figure 7 we present the sum of our spectra in units of photons cm^{-2} s^{-1} Å^{-1} versus wavelength. Note that because of a larger uncertainty in the flux calibration at long wavelength, we have attenuated the flux measured at 650 Å by the ISM hydrogen absorption (assuming a column of 10^{18} cm^{-2}) to extrapolate the flux at wavelengths greater than 650 Å. We also present the H I, He I, and He II photoionization cross sections. Using these data, we estimate the following photoionization parameters:

$$\Gamma_{\mathrm{H\,II}} = 1.94 \times 10^{-16}\ \mathrm{s}^{-1}\,,$$
$$\Gamma_{\mathrm{He\,II}} = 5.46 \times 10^{-16}\ \mathrm{s}^{-1}\,,$$
$$\Gamma_{\mathrm{He\,III}} = 2.81 \times 10^{-17}\ \mathrm{s}^{-1}\,. \qquad (1)$$

These photoionization parameters may be added to previous investigations and used to predict ionization levels. They already indicate a very low rate of ionization of He II−> He III in comparison with the other rates.

3.4. *Influence of Metal Opacities*

The use of EUV emission from hot DA stars as background sources for probing the ISM is complicated by the possible presence of photospheric heavy elements that will affect the continuum level in these objects. *EUVE* spectroscopy allows us to account properly for this effect. While Feige 24, G191-B2B, and MCT 0455−2812 depart significantly from a pure hydrogen spectrum at short wavelengths because of the influence of heavy elements (as demonstrated in Fig. 1), the spectra do appear well modeled between 400 and 600 Å by pure hydrogen models, as demonstrated in § 3.2. However, if we study broader spectral ranges, we find the continuum shape of a blanketed model spectrum strongly distorted relative to a pure hydrogen model, resulting in a flux deficit at short EUV wavelengths ($\lambda \leq 240$ Å) and a steep *absolute* flux increase at longer wavelengths, particularly near 504 Å. We show in Figure 8 a comparison over the complete EUV range of a pure hydrogen model and a heavy element blanketed model at $T_{\mathrm{eff}} = 60{,}000$ K and $\log g = 7.5$. The spectra are normalized to the visual magnitude of G191-B2B and clearly illustrate the flux downturn near 240 Å and the flux increase above 300 Å from a backwarming effect. We have noted in Figure 8 that, for a given effective temperature, the flux in the 400–600 Å region is 60% higher for the metal-blanketed model.

To assess the potential effect of additional photospheric opacities in hot white dwarf atmospheres on the H I and He I column density determinations, we have reevaluated our solutions presented in § 3.2 for G191-B2B, Feige 24, and MCT 0455−2812. We apply the techniques described in § 3.2 but use

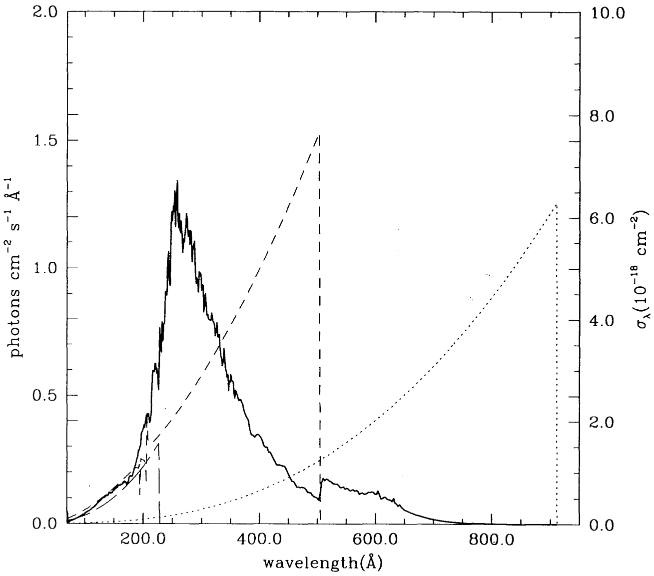

FIG. 7.—Total EUV flux from our sample white dwarfs (*solid line*) compared to photoionization cross sections of H I (*short-dashed line*), He I (*medium-dashed line*), and He II (*long-dashed line*).

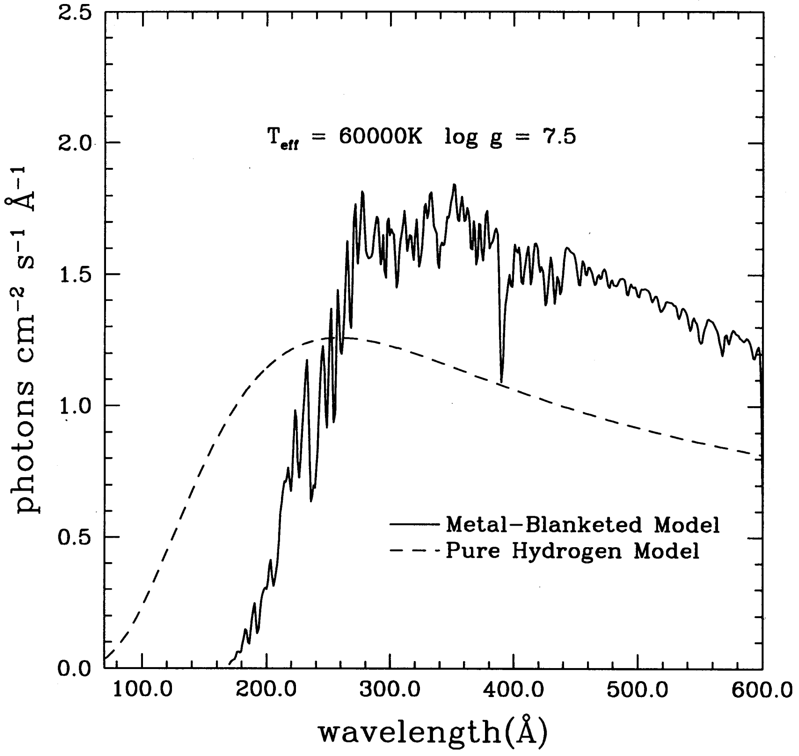

FIG. 8.—Blanketing effect of a trace abundance of heavy elements on the Lyman continuun of hot DA stars. A comparison is made betwen a pure hydrogen model (*dashed line*) and a model computed with a mixture of heavy elements (*solid line*) both normalized at the *V* magnitude of G191-B2B. In the latter case, the flux is systematically higher than the flux predicted by a pure hydrogen model by 60% over the range of interest (400 ≤ λ ≤ 600 Å).

blanketed model spectra, and we show the results for G191-B2B in Figures 9*a*–9*b*, for Feige 24 in Figures 10*a*–10*b*, and for MCT 0455−2812 in Figures 11*a*–11*b*. The derived hydrogen column densities are higher by about 10% than the values determined from pure hydrogen models to compensate for the stronger Lyman-continuum flux. The helium column densities are not significantly altered; this has the effect of decreasing the abundance ratio of He I to H I in the LISM as listed in Table 2, where we compare the values derived using our two grids of models (labeled "pure-H" and "H+CNOFe"). We have also found that the effective temperature that fits the Lyman continuum is about 4000 K cooler than the one obtained from a fit of a pure hydrogen model. This fit indicates the potentially important effect of neglected heavy element opacities in models commonly used in the analysis of optical spectra of hot DA stars. A similar effect caused by undetected helium was pointed out by Bergeron et al. (1994). Clearly, the combined effects of

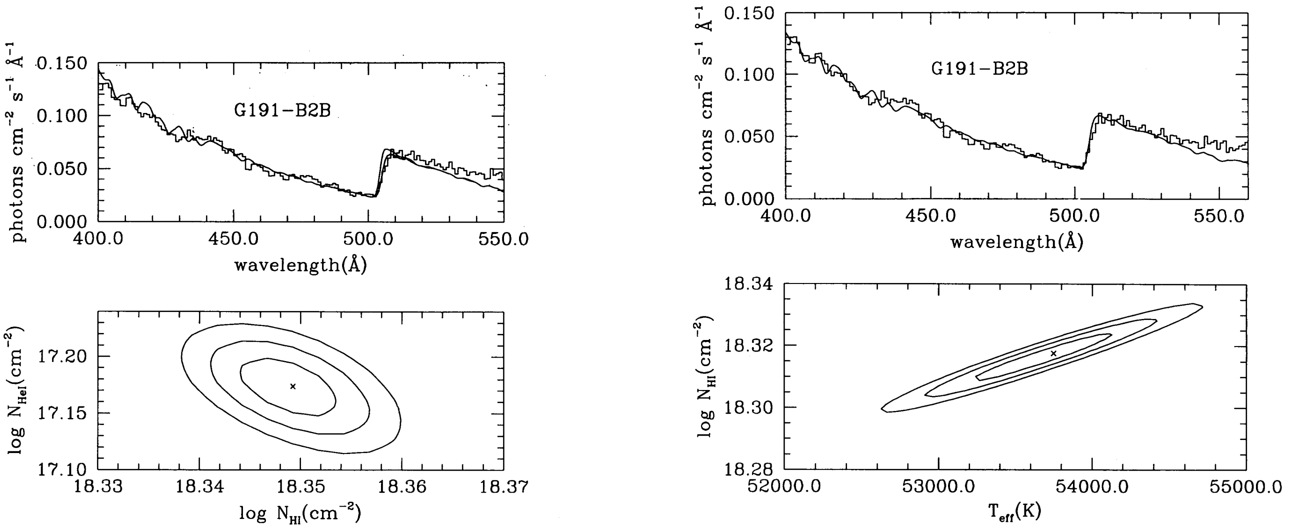

FIG. 9*a*

FIG. 9*b*

FIG. 9.—(*a*) Same as Fig. 4*a*, but with a minimum χ^2 fit of the Lyman continuum of G191-B2B with a model spectra including heavy element opacities. (*b*) Same as Fig. 5*a*, but with a minimum χ^2 fit of the Lyman continuum of G191-B2B with a model spectra including heavy element opacities.

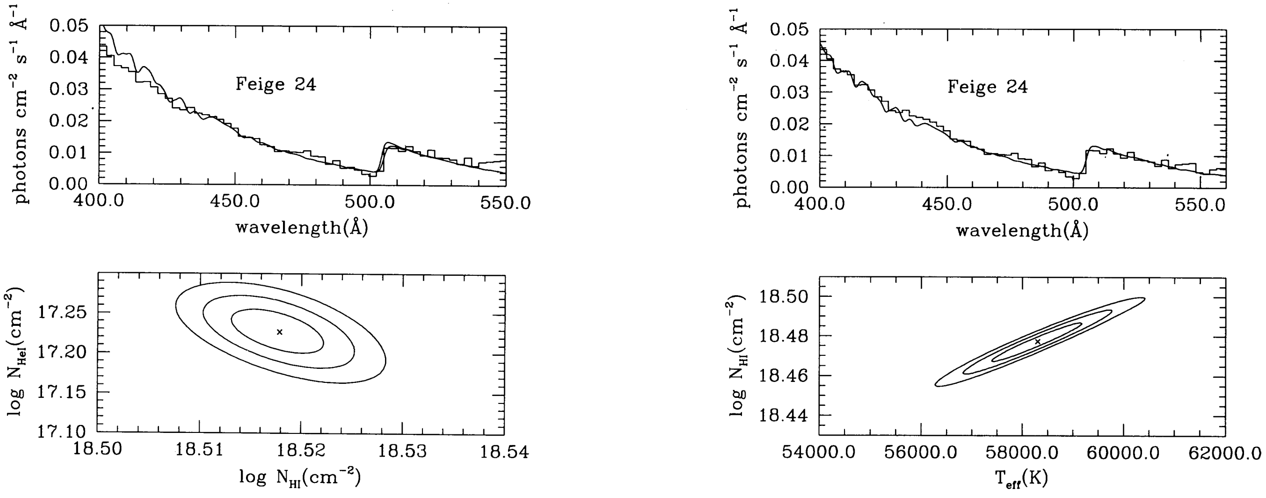

FIG. 10*a* FIG. 10*b*

FIG. 10.—(*a*) Same as Fig. 9*a*, but for Feige 24. (*b*) Same as Fig. 9*b*, but for Feige 24.

helium and traces of heavier elements will have to be taken into account when defining the temperature scale of hot white dwarfs.

4. CONCLUSIONS

We have analyzed EUV spectra of six hot hydrogen-rich white dwarfs obtained as part of NASA's *Extreme-Ultraviolet Explorer* Guest Investigator Program. We have demonstrated that at least three objects in our sample (Feige 24, G191-B2B, and MCT 0455−2812) show clear spectroscopic signatures of heavy elements (possibly carbon, nitrogen, oxygen, and iron) at wavelengths shorter than 300 Å, but that at longer wavelengths these spectra do not show effects of these elements and are suitable for studies of the LISM. We have determined that the atmospheres of HZ 43, GD 153, and GD 71 are consistent, to a high degree, with pure-hydrogen atmospheres. This pattern confirms earlier descriptions of the spectral properties of hot white dwarf stars (see Vennes et al. 1989; Vennes 1992; Vennes & Fontaine 1992) and exposes serious theoretical shortcomings encountered in the study of heavy element abundance in hot white dwarf stars. Chayer, Fontaine, & Wesemael (1995) and Chayer et al. (1995) demonstrate that the relatively pure atmospheres of some white dwarf stars, HZ 43 and GD 153 in particular, cannot be explained in the context of diffusive equilibrium and that a weak mass loss may have purified their atmospheres. Finally, we have measured stellar effective temperatures based on EUV continuum properties. These new estimates are compared with optical and far-ultraviolet temperature measurements, and we find that the presence of heavy elements strongly affects the determination of this parameter in the cases of Feige 24, G191-B2B, and MCT 0455−2812. We confirm earlier temperature determinations based on *EUVE* photometry presented by Vennes et al. (1994).

We have determined column densities of neutral hydrogen and helium in six lines of sight, as well as upper limits to ionized helium column densities. Our column measurements of the neutral species indicate a relatively higher degree of ionization in the LISM of helium relative to hydrogen assuming prior knowledge of their cosmic abundance ratio ($n_H/n_{He} = 10$). Using the upper limits to the ionized helium column, we have

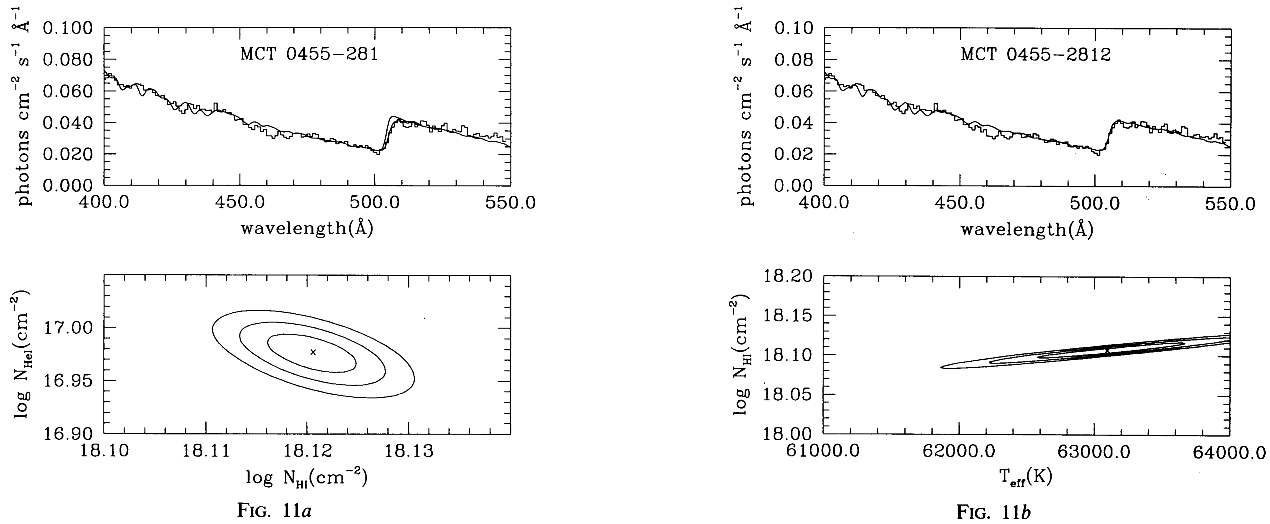

FIG. 11*a* FIG. 11*b*

FIG. 11.—(*a*) Same as Fig. 9*a*, but for MCT 0455−2812. (*b*) Same as Fig. 9*b*, but for MCT 0455−2812.

placed upper limits to the absolute degree of ionization of these two elements; reasonable variations around the cosmic abundance ratio do not alter our conclusion that hydrogen is not appreciably ionized in the LISM in at least two lines of sight (HZ 43 and GD 153). Extreme-ultraviolet spectroscopy of hot white dwarf stars is the only direct probe of hydrogen and helium column densities in the local interstellar medium.

This research is supported by NASA contract NAS 5-30180 and NASA grant NAG 5-2405 (J. D., S. V., S. B.), by a NSF grant PHY-911505597 (A. K. P.), and by the Carlsberg Foundation, Niels Bohr Institute, and the SDCN computing center in Sweden (P. T.). We would like to thank Andrea Frank and the editorial staff at the Center for EUV Astrophysics for helping improve the manuscript.

APPENDIX A

REDUCTION OF FIXED PATTERN NOISE

The microchannel plate (MCP) detectors used with the *EUVE* spectrometer are known to exhibit pseudoperiodic small spatial scale variations in response to uniform illumination. On flat-field images obtained during the laboratory calibration of the detectors, they appear as a hexagonal pattern corresponding to the boundary of the multifiber bundles forming the MCP (Vallerga et al. 1989, 1991). Cross sections of the flat-field images show modulation with respect to the average that can reach an amplitude of up to 20% on a spatial scale of roughly 500 μm (approximately 17 pixels for 2048 × 2048 pixel *EUVE* spectrometer images). It is believed that these variations are caused by a slight shift in the registration of the centroids of the electron clouds transferred near the fiber bundles boundary. Flux is conserved, since no events are lost but are recorded at a location slightly offset from their true physical locations. This small-scale variation in the detector response will mainly affect the spectra of EUV continuum sources for which the signal-to-noise ratio will be comparable to or greater than the typical fixed pattern noise amplitude (that is, for signal-to-noise ratios greater than about 10). A common procedure used in astronomy to remove small-scale variations on a detector is to obtain flat-field images at a high signal-to-noise ratio. Unfortunately, the flat fields obtained during the ground calibration cannot be applied to in-orbit observations because of either differences in detector operation parameters or insufficient counting statistics. Also, no known astrophysical sources allow for a uniform illumination of the full detector surfaces that would provide a usable in-orbit flat field in a practical exposure time.

Important progress has been made in the removal of fixed pattern noise from *EUVE* spectra. The pointing stability of *EUVE* (less than 8″ rms, 1 pixel is about 4″.4) implies that the fixed pattern noise is not smeared out by the spacecraft pointing jitters. In the absence of a flat field, the alternative method developed to smooth the fixed pattern noise forces the spacecraft to point at several random directions during an observation within an error circle matching the size of the hexagonal pattern (radius < 2′). Observations of Feige 24, G191-B2B, MCT 0455−2812, and HZ 43 were obtained with several short duration (one- or two-orbit) pointings slightly offset from the boresight to explore the performance of the procedure. The final images are corrected using the aspect solution. The quality of the wavelength solution and the spectral resolution are not noticeably degraded for pointings within

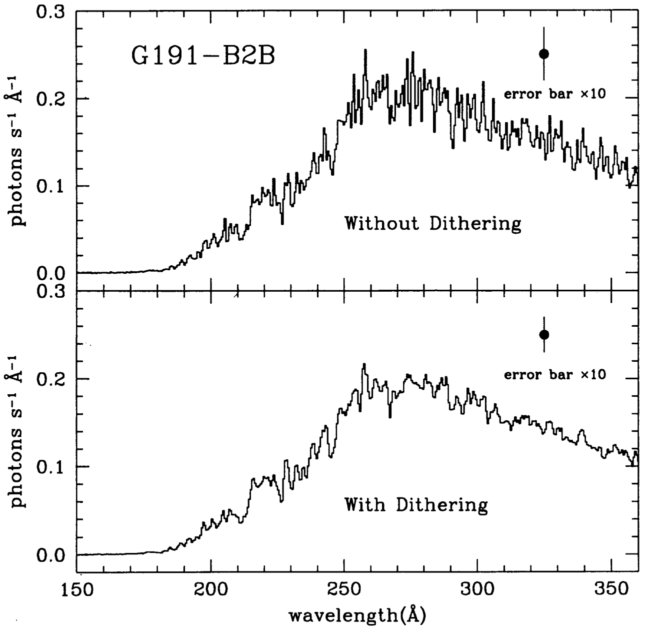

FIG. 12

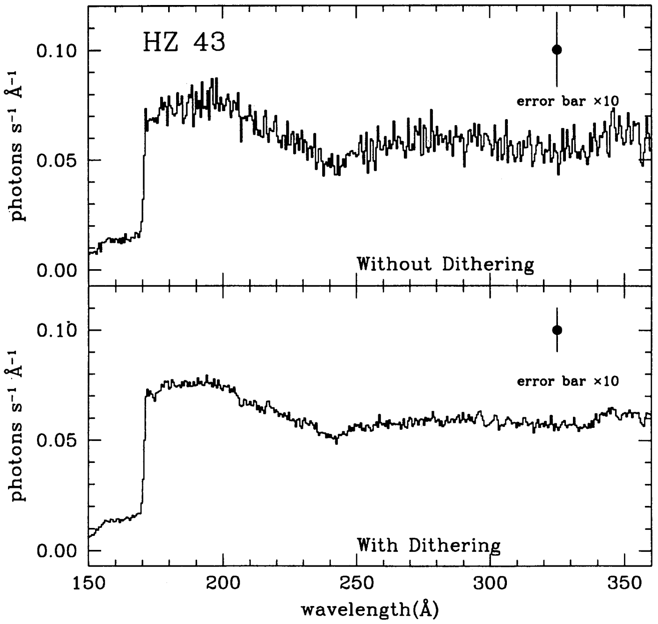

FIG. 13

FIG. 12.—A comparison between the dithered and the nondithered spectra of G191-B2B (see text)
FIG. 13.—A comparison between the dithered and the nondithered spectra of HZ 43 (see text)

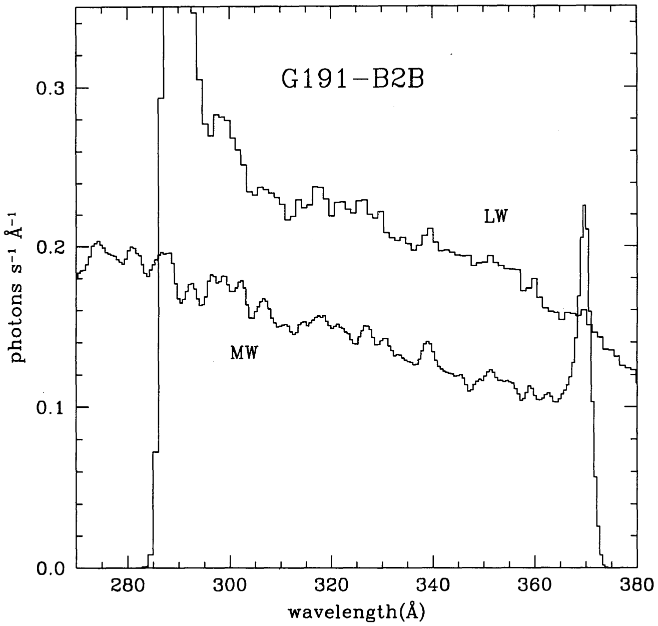

FIG. 14.—Coincidence between the absorption features detected within the overlap of the medium-wavelength and long-wavelength dithered spectra of G191-B2B.

2′ from boresight (Jelinsky, Abbott, & Boyd 1994). In Figures 12 and 13 we show a comparison between the dithered and nondithered spectra of G191-B2B and HZ 43. Each observation had sufficiently long exposure times that the photon noise was relatively small as illustrated by the size of the error bars (which are multiplied by 10). Nondithered observations have produced noisier spectra than expected on the basis of photon counting statistics. In a spectrum like G191-B2B that is expected to exhibit metallic absorption lines and photoioization edges, this effect makes it difficult to identify any of the real features. In contrast, dithered spectra have a much cleaner appearance, and in fact most of the apparent absorption features have vanished. The features left in the G191-B2B spectrum are most certainly real. An indication of the reality of the remaining features is strongly suggested by comparing the overlap between the MW and LW spectra, which we show in Figure 14. We find an excellent correspondence between the features detected in the MW and LW, where some of the departures can be explained by the difference in spectral resolution. The HZ 43 dithered spectrum is also showing weak absorption features that could be real but that could also be residual from the fixed pattern noise. We estimate the improvement in the signal-to-noise ratio from the observations of HZ 43 to be around a factor of 4 (S/N $\approx$ 5 for nondithered and $\approx$20 for dithered).

APPENDIX B

DETERMINATION OF THE EFFECTIVE AREAS OF THE LW SPECTROMETER

As discussed in § 2, the *EUVE* spectra are contaminated by overlapping spectral orders. This is especially true for the LW spectrometer, where the spectrum can be severely contaminated over the complete bandpass by the second, third, and fourth spectral orders, and obvious errors will be introduced if these contributions are ignored. Many measurements rely on the absolute value of the flux in the Lyman continuum as well as on the flux ratio on both sides of the photoionization edge of He I. We have therefore explicitly determined the LW high-order effective areas by using spectra of bright white dwarfs having ISM hydrogen column densities sufficiently high that no first-order detections occur in essentially the entire LW spectrometer. Two stars were selected for this work, GD 246 (WD 2309+105) and EUVE J2214−491. Spectra of these stars are shown in the LW band in Figures 15 and 16.

The determination of the true effective area is done by converting the MW spectrum into flux units by dividing the extracted spectrum by the exposure time, the bin size, and the first-order effective area of the MW spectrometer. Note that MW spectra are also contaminated by overlapping orders but to less extent and mostly at the very end of the MW range ($\geq$340 Å). Nonetheless, this effect was taken into account in the MW conversion to flux units. Then we use the flux measured in the MW spectrometer to predict the contribution of each spectral order in the LW spectrometer by taking the product between the MW flux and the respective high-order effective area curves. The wavelengths are assigned by multiplying the MW wavelengths by the order number, and the MW flux is divided by the order number to account for the stretch of the wavelength scale. A comparison with the LW spectra of GD 246 and EUVE 2214−491 indicates that the current higher order effective areas predict a somewhat higher count rate than what is really observed, showing that some correction must be applied to the higher order effective areas in the LW. We assume that the shape of the effective area curves is correct, and we derive a gray correction factor that will minimize the discrepancy with the

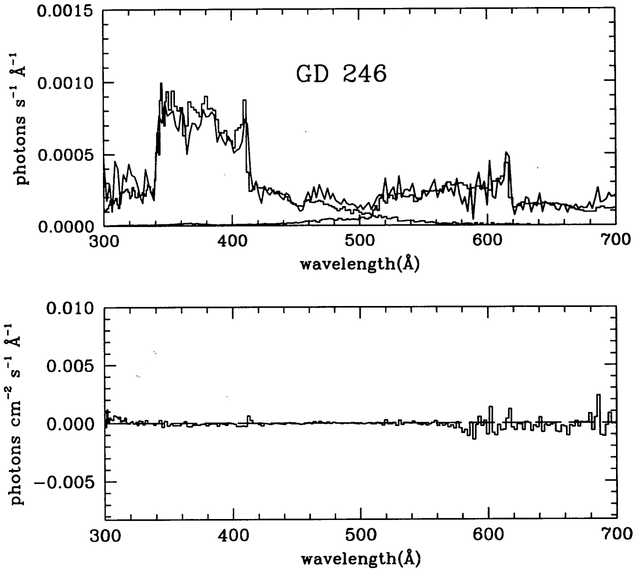

FIG. 15

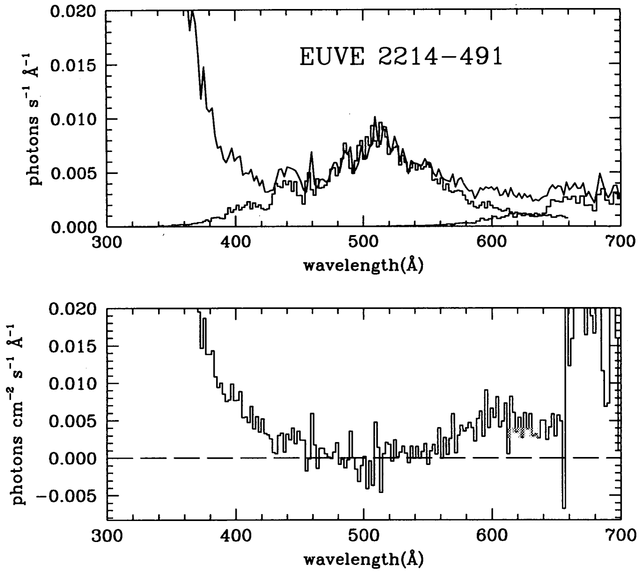

FIG. 16

FIG. 15.—Subtraction of the second- and third-order spectra in the long-wavelength spectra of the DA white dwarf GD 246 using *corrected* higher order effective areas.

FIG. 16.—Same as Fig. 15, but for the DA white dwarf RE 2214−491

observed orders. We have determined, based on GD 246 and EUVE 2214−491, that the second-order effective areas should be divided by a gray correction factor equal to 1.4, while the third and fourth orders should be divided by the somewhat smaller correction factors of 1.2 and 1.1, respectively. This particular combination of correction factors provides a good basis for the subtraction of orders up to a wavelength of about 560 Å, as illustrated in Figures 15 and 16. At wavelengths longer than 560 Å, it becomes increasingly difficult to separate the orders, and therefore one should treat the resultant flux with more caution in the last third of the LW range. In this paper, we take this situation into account by restricting the fitted region to wavelengths short of 550 Å. Strictly speaking, this empirical technique establishes the ratio of the effective areas in the MW in the first order to the LW in higher orders (we assume that the first-order MW effective area is correct). Nonetheless, we obtain an entirely self-consistent prediction of the higher order effects.

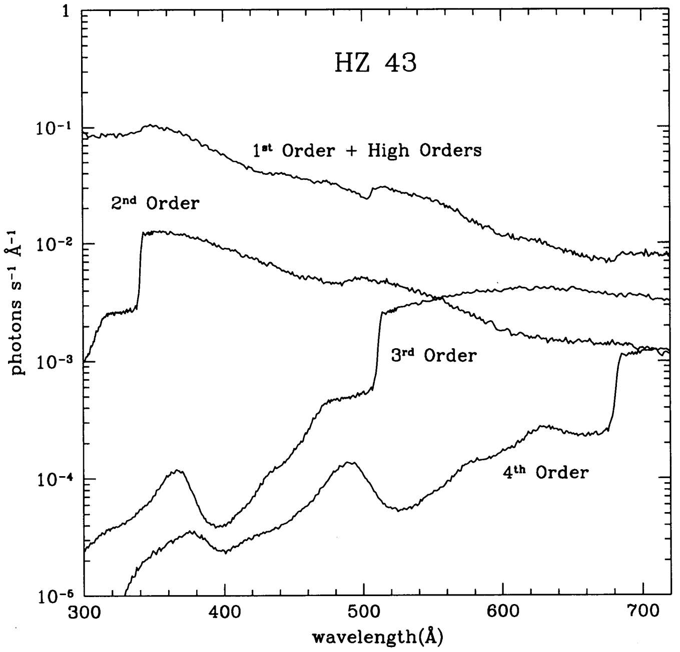

FIG. 17

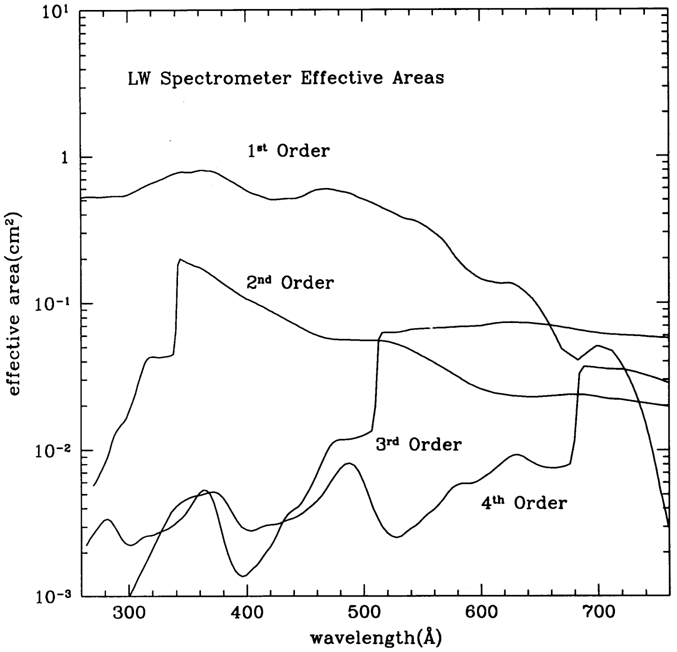

FIG. 18

FIG. 17.—Decomposition of HZ 43's long-wavelength spectrum in its first- to fourth-order components

FIG. 18.—Long-wavelength spectrometer effective areas in the first to fourth order

We apply this technique to predict the second-order spectra contribution to the LW spectra of HZ 43. We show in Figure 17 the LW spectra of HZ 43 along with the contribution of the higher spectral orders. In both cases, their contribution to the total spectrum is not negligible and becomes progressively important toward longer wavelengths. Finally, we present the adopted effective areas in Figure 18.

REFERENCES

Barstow, M. A., et al. 1994, MNRAS, 267, 647
Bergeron, P., Wesemael, F., Beauchamp, A., Wood, M. A., Lamontagne, R., Fontaine, G., & Liebert, J. 1994, ApJ, 432, 305
Bowyer, S., Lieu, R., Lampton, M., Lewis, J., Wu, X., Drake, J. J., & Malina, R. F. 1994, ApJS, 93, 569
Chayer, P., Fontaine, G., & Wesemael, F. 1995, ApJS, 99, 189
Chayer, P., & Vennes, S. 1995, in preparation
Chayer, P., Vennes, S., Pradhan, A. K., Thejll, P. A., Beauchamp, A., Fontaine, G., & Wesemael, F. 1995, ApJ, 454, 429
Cheng, K.-P., & Bruhweiler, F. C. 1990, ApJ, 364, 573
Frisch, P. C., Welty, D. E., York, D. G., & Fowler, J. R. 1990, ApJ, 357, 514
Green, J., Jelinsky, P., & Bowyer, S. 1990, ApJ, 359, 499
Grevesse, N. & Noels, A. 1993, in Origin and Evolution of the Elements, ed. N. Prantzos, E. Vangioni-Flam, & M. Cassé (Cambridge: Cambridge Univ. Press), 15
Heise, J., Paerels, F. B. S., Bleeker, J. A. M., & Brinkman, A. C. 1988, ApJ, 334, 958
Hettrick, M. C., Bowyer, S., Malina, R. F., Martin, C., & Mrowka, S. 1985, Appl. Opt., 24, 1737
Holberg, J. B., Sandel, B. R., Forrester, W. T., Broadfoot, A. C., Shipman, H. L., & Barry, J. L. 1980, ApJ, 242, L119
Holberg, J. B., Wesemael, F., & Basile, J. 1986, ApJ, 306, 629
Hurwitz, M. & Bowyer, S. 1995, ApJ, 446, 812
Jelinsky, P., Abbott, M., & Boyd, B. 1994, *EUVE* internal report
Kimble, R. A., et al. 1993a, ApJ, 404, 663
———. 1993b, ApJ, 408, L41
Lallement, R., Bertin, P., Ferlet, R., Vidal-Madjar, A., & Bertaux, J. L. 1994, A&A, 286, 898
Lampton, M., Margon, B., & Bowyer, S. 1976, ApJ, 208, 177
Napiwotzki, R., Barstow, M. A., Fleming, T. A., Holweger, H., Jordan, S., & Werner, K. 1993, A&A, 278, 478
Reynolds, R. J. 1986, AJ, 92, 653
Rumph, T., Bowyer, S., & Vennes, S., 1994, AJ, 107, 2108
Sciama, D. W. 1991, A&A, 245, 243
Seaton, M. J., Yan, Y., Mihalas, D., & Pradhan, A. K. 1994, MNRAS, 266, 805
Slavin, J. D. 1989, ApJ, 346, 718
Theodosiou, C. E. 1987, At. Data Nucl. Data Tables, 36, 97
Vallerga, J. V., Gibson, J. L., Siegmund, O. H. W., & Vedder, P. W. 1989, Proc. SPIE, 1159, 382
Vallerga, J. V., Sigmund, O. H. W., Vedder, P. W., & Gibson, J. L. 1991, Nucl. Instrum. Methods Phys. Res., 310, 317
Vennes, S. 1992, ApJ, 390, 590
Vennes, S., Chayer, P., Fontaine, G., & Wesemael, F. 1989, ApJ, 336, L25
Vennes, S., Chayer, P., Thorstensen, J. R., Bowyer, S., & Shipman, H. L. 1992, ApJ, 392, L27
Vennes, S., Dupuis, J. Bowyer, S., Fontaine, G., Wiercigroch, A., Jelinsky, P., Wesemael, F., & Malina, R. F. 1994, ApJ, 421, L35
Vennes, S., Dupuis, J., Rumph, T., Drake, J. J., Bowyer, S., Chayer, P., & Fontaine, G. 1993, ApJ, 410, L119
Vennes, S., & Fontaine, G. 1992, ApJ, 401, 288
Vennes, S., Pradhan, A. K., & Thejll, P. 1995, in preparation
Vennes, S., Thejll, P., & Shipman, H. L. 1991, in White Dwarfs, ed. G. Vauclair & E. Sion (Dordrecht: Kluwer), 235